ACS NANO

www.acsnano.org

Resolving the Conflict between Strength and Toughness in Bioactive Silica–Polymer Hybrid Materials

Wei Fan, Tao Du, Aida Droce, Lars R. Jensen, Randall E. Youngman, Xiangting Ren, Leonid Gurevich, Mathieu Bauchy, Peter Kristensen, Bengang Xing, Donghong Yu,* and Morten M. Smedskjaer*

Cite This: *ACS Nano* 2022, 16, 9748–9761

Read Online

ACCESS | Metrics & More | Article Recommendations | Supporting Information

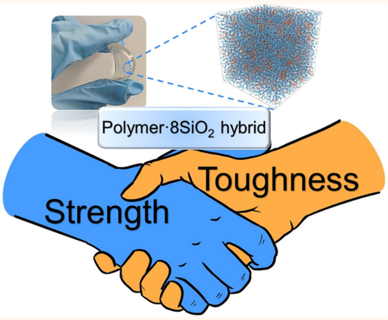

ABSTRACT: **Simultaneously improving the strength and toughness of materials is a major challenge. Inorganic–polymer hybrids offer the potential to combine mechanical properties of a stiff inorganic glass with a flexible organic polymer. However, the toughening mechanism at the atomic scale remains largely unknown. Based on combined experimental and molecular dynamics simulation results, we find that the deformation and fracture behavior of hybrids are governed by noncovalent intermolecular interactions between polymer and silica networks rather than the breakage of covalent bonds. We then attempt three methods to improve the balance between strength and toughness of hybrids, namely the total inorganic/organic (I/O) weight ratio, the size of silica nanoparticles, and the ratio of –C–O *vs* –C–C bonds in the polymer chains. Specifically, for a hybrid with matched silica size and I/O ratio, we demonstrate optimized mechanical properties in terms of strength (1.75 MPa at breakage), degree of elongation at the fracture point (31%), toughness (219 kPa), hardness (1.08 MPa), as well as Young's modulus (3.0 MPa). We also demonstrate that this hybrid material shows excellent biocompatibility and ability to support cell attachment as well as proliferation. This supports the possible application of this material as a strong yet tough bone scaffold material.**

KEYWORDS: *silica–polymer hybrid, strength toughness balance, atomic-scale predicting, simulation, bioactive materials*

INTRODUCTION

The conflict between strength and toughness in materials continues to have important consequences for various structural and functional applications, despite the progress that has been made.[1,2] Strength represents the largest achievable stress in the material, whereas toughness is the material's resistance to fracture when a crack is present.[3] Materials that can dissipate high local stresses by undergoing limited deformation are tough, which explains why strong materials, *i.e.*, those that deform less readily, tend to be brittle.[1] For instance, oxide glasses can reveal high fracture strength above 10^2 MPa but typically are less tough and flexibile,[4] while polymer hydrogel materials can be stretched to several times their original length but at the same time exhibit low fracture strength in the range of tens to hundreds of kPa.[5] Such strong-but-brittle or tough-but-weak materials are unsuitable for accommodating cyclic loading in a wide range of applications, including those within soft robotics and tissue regeneration. Balancing strength and toughness is thus urgently needed to satisfy the aforementioned requirements. Strategies based on, for instance, double-network polymers[6] and binary/ternary systems[7] have been attempted. However, all-polymer systems with desirable flexibility could hardly reach the strength requirements for applications *in vivo*, since native human articular cartilage has a compression modulus of about 0.4–2.0 MPa.[8,9] On the other hand, binary or ternary systems usually suffer from phase separation and undesirable synergetic properties, which hinder many possible applications.[10]

To overcome the conflict of strength *vs* toughness and avoid issues with phase separation, a promising method would be the synthesis of covalently linked inorganic–polymer hybrid materials[11−13] since such hybrid materials can synergistically combine the advantages of flexible polymers and rigid inorganic glass networks.[14−16] In some cases, such inorganic–polymer hybrids have been reported to feature excellent

Received: April 8, 2022
Accepted: June 6, 2022
Published: June 9, 2022

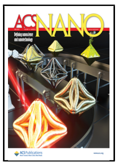

https://doi.org/10.1021/acsnano.2c03440

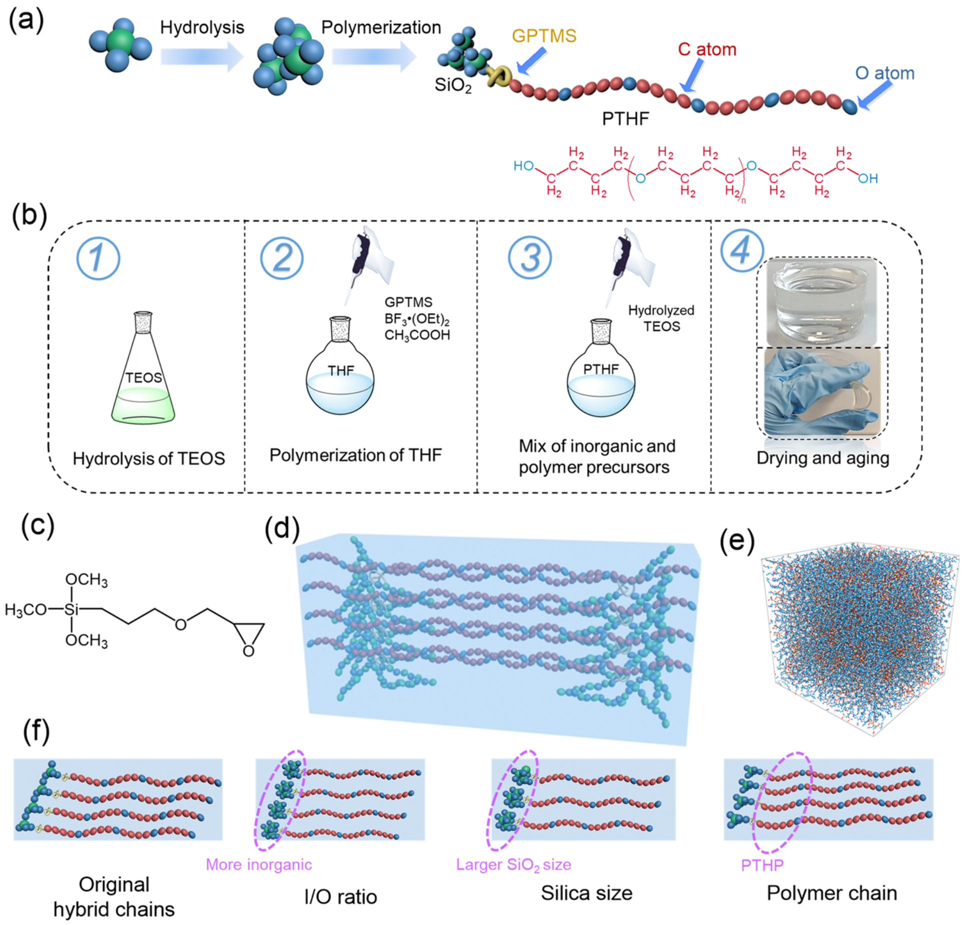

Figure 1. (a) Schematic structure of hybrid: the silica network is covalently bonded to polymer chains *via* coupling agents and the molecular structure of PTHF; (b) synthesis process and obtained flexible and optically transparent PTHF·*x*TEOS hybrids; (c) molecular structure of coupling agent GPTMS; (d) schematic 3D-structure of a hybrid bulk; (e) MD simulated 3D-structure of a hybrid bulk where the color of the atoms matches that of panel (a); and (f) schematic structures of hybrids with different I/O weight ratio, silica size, and polymer repeating unit.

functional and mechanical properties, making them suitable for bio-related applications as mentioned above.[17−19] To ensure the integrity of the hybrids at the atomic scale, covalent bonding between the two phases to form interpenetrating hybrid co-networks is usually achieved *via* organic−inorganic coupling agents.[20] Different organic silane coupling agents are widely applied as they can adapt to various reaction mechanisms for constructing covalent bonds between silica and polymers.[21−23] For example, coupling agents such as vinyltriethoxysilane, diethoxydivinylsilane, and diethoxymethylvinylsilane with vinyl functional groups can react with other vinyl monomers *via* a free-radical polymerization mechanism,[24,25] while the epoxide group of glycidoxypropyl trimethoxysilane (GPTMS) can participate in a ring-opening process with suitable cyclic ether monomers.[26−29] In turn, the silyl group on the latter can react with tetraethyl orthosilicate (TEOS) as the inorganic precursor through sol−gel condensation process. This enables the inorganic component to bond to organic polymer chains and thus promote its uniform dispersion in the hybrid network to avoid phase aggregation and separation.[29,30] As such, the amount of silane coupling agent determines the number of covalent links between the silica sub-network and the polymer chains.[27,28]

Hydrolyzed TEOS bonds to polymer chains in such systems and can be used to control the size of the silica nanoparticles and total inorganic-to-organic (I/O) ratio.[27] In addition, varying the structure of the polymer backbone is another path to adjust the mechanical properties of hybrids.[28] Due to their controllable structures and polymerization mechanism, epoxides and other cyclic ether monomers are good candidates for forming the polymer backbone.[29] As a thermoplastic, polytetrahydrofuran (PTHF) is commonly applied for biomedical applications due to its desirable anticoagulant abilities when incorporating polyurethane[30,31] *via* cationic ring opening approach, giving rise to bulk materials with bouncy and tough mechanical performance.[25] Similar monomers such as ethylene oxide and tetrahydropyran undergo the same polymerization mechanisms,[27] but with different ratio of C−O to C−C bonds, thus enabling further control of the hybrid structure and mechanical properties at the molecular level.[29,32]

To understand the changes in the structure of such hybrid materials at the atomic scale *in situ* during deformation and fracture, molecular dynamics (MD) simulations are needed. This is necessary since *in situ* mapping of atomic rearrangements during fracture is still out of reach experimentally. MD simulations have previously been used to understand the fracture behavior of various materials, including epoxy resins,[33] oxide glasses,[34] nanocomposites,[35] *etc*. However, such simulations have not yet been applied to understand the mechanical properties of hybrids with systematically varying components.

https://doi.org/10.1021/acsnano.2c03440

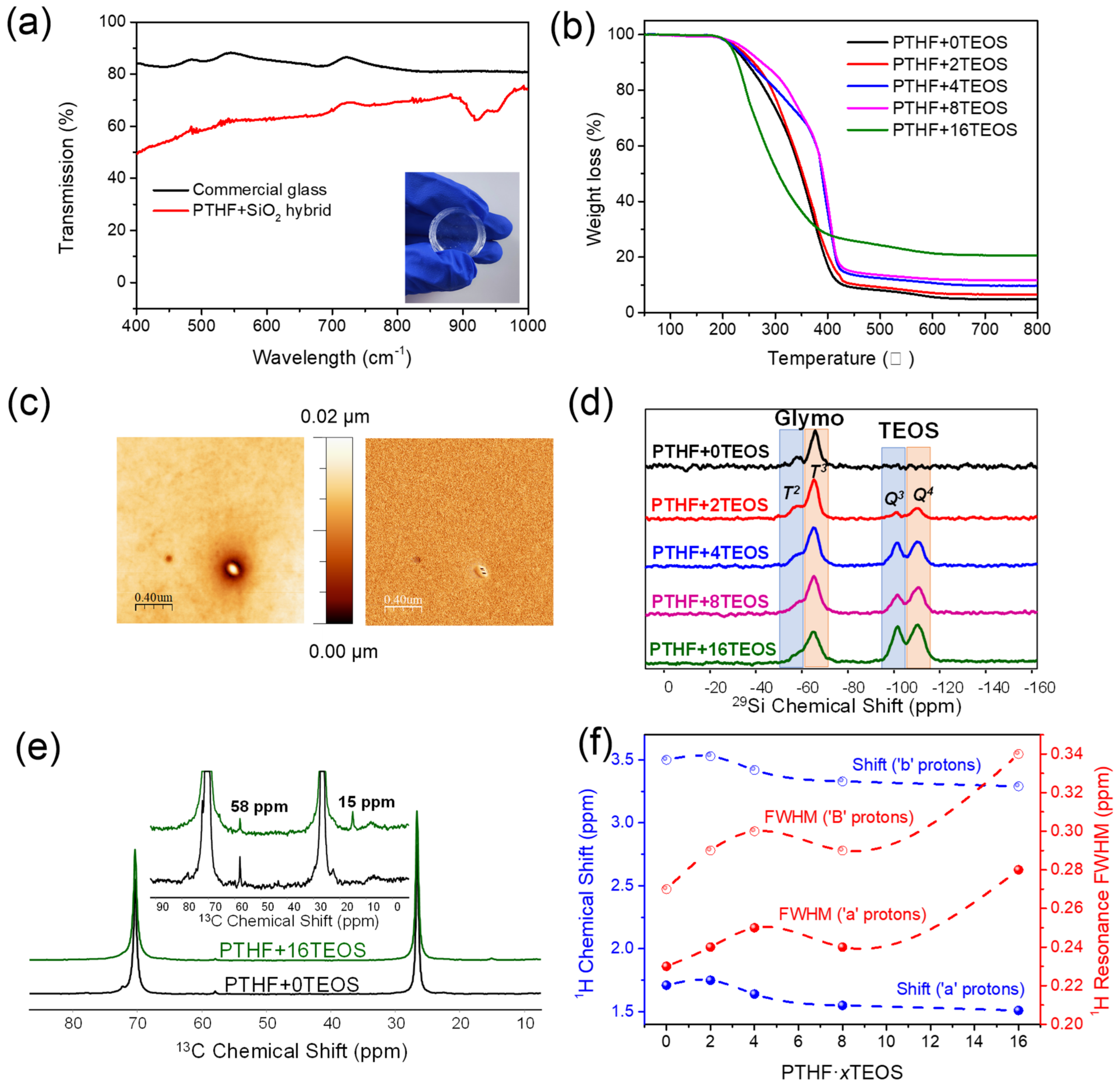

Figure 2. (a) UV−vis transmission spectra of the PTHF·8TEOS hybrid sample as well as commercial soda−lime−silica glass, both with a thickness of 5 mm. (b) TGA heating curves of hybrids with varying I/O ratios, *i.e.*, the series of PTHF·*x*TEOS hybrids. (c) Height (left) and phase (right) AFM images of the hybrid PTHF·16TEOS. (d) ^{29}Si and (e) ^{13}C spectra of PTHF·*x*TEOS hybrids. (f) FWHM (full width at half-maximum) and chemical shift for ^{1}H peaks in PTHF structures. The names and compositions of these hybrid samples are given in Table 1.

In this work, we systematically investigate the mechanism of deformation and fracture of inorganic−polymer hybrid materials at the atomic scale using a combination of experiments and MD simulations. Specifically, we attempt to control the noncovalent intermolecular interactions in the hybrids by varying the size of silica nanoparticles (NPs), fraction of C−O bonds in hybrids, and total organic−inorganic weight ratios. Based on these systematic studies, we successfully achieved an improved balance of toughness and strength (or flexibility and hardness) in a hybrid PTHF·8TEOS that can be compressed to 31% compared with its original height for a strength of 1.75 MPa at breakage and toughness of 219 kPa. Importantly, we show that these hybrids reveal excellent biocompatibility, including noncytotoxicity and the ability to support cell attachment as well as further cell proliferations. Overall, our study shows that by understanding the hybrid deformation and fracture mechanism it is possible to control the hybrids' mechanical properties. These findings could enable applications of such tailorable inorganic−polymer hybrids within tissue engineering and soft robotics.

RESULTS AND DISCUSSION

Synthesis of Hybrid Materials. As shown schematically in Figure 1a, silica and PTHF backbones were covalently linked through the silane coupling agent GPTMS.[25,27] The synthesis combines a sol−gel method for preparation of the SiO$_2$ precursor with cationic ring-opening processes for the organic monomers (Figure 1b). Specifically, TEOS was first hydrolyzed, generating −OH groups (see steps 1 and 2 in

Figure 1b), and second co-condensed, leading to covalent links between SiO_2 and organic polymers (see step 3 in Figure 1b). Then, upon initiation by the Lewis acid $BF_3{\cdot}(OEt)_2$, the oxirane group of GPTMS (Figure 1c) started the ring-opening polymerization of THF monomers, resulting in covalent links between the phases in the hybrid after prolonged condensation and drying (see step 4 in Figure 1b).[25,36] The hydrolysis process, polymerization mechanism, and molecular structures of such PTHF−SiO_2 hybrids are presented in Figure S1.[27] As we will show in this study, the obtained hybrids inherit the advantages of flexible polymers and hard inorganic components but also exhibit good transparency (Figure 1b). We combine experimental methods and MD simulations (Figure 1d,e) and perform systematic investigations of three compositional effects on the hybrid structure and mechanical properties, namely (Figure 1e): (i) varying amount of TEOS for the same content of GPTMS and PTHF (leading to different I/O weight ratios, in PTHF·xSiO$_2$ series of hybrids) in experiments and MD simulations; (ii) varying molar ratios of TEOS-to-GPTMS under a constant I/O weight ratio (resulting in differences in the silica size, in y·GPTMS:z·TEOS series of hybrids) in experiments; and (iii) varying polymer chain repeating unit (PTHF *vs* PTHP (poly tetrahydropyran)) in MD simulations. Regarding the TEOS-to-GPTMS variation for series ii, we note that since GPTMS is the only compound herein that can form covalent links between the organic and inorganic components the amount of GPTMS determines the number of covalently linked silica particles in the system and thus their size. We also note that hybrid series iii is only done in simulations due to the difficulty in polymerizing PTHP, but it allows us to gain fundamental understanding of the role of varyiation on the C−O to C−C bond ratio on the hybrids' mechanical properties.

Experimentally Produced Hybrids with Different I/O Ratio. Considering first the PTHF·xTEOS (x = 0, 2, 4, 8, 16) hybrids, we find that after drying and aging processes the hybrids possess high visual transparency (see inset of Figure 2a). Ultraviolet−visible (UV−vis) spectroscopy measurements are performed to quantify the optical transparency of the hybrid PTHF·8TEOS and make a comparison with a commercial soda−lime−silica glass.[37] Both hybrid and glass samples have a thickness of 5 mm. As shown in Figure 2a, the transparency of the hybrid is up to around 70% over a wide wavelength range of 400 to 1000 nm. Next, to understand the molecular structures of the PTHF·xTEOS series of hybrids, Fourier transform infrared (FT-IR) absorption spectra were recorded, as shown in Figure S2. The bands at 490 and 1090 cm^{-1} correspond to characteristic Si−O−Si asymmetric stretching vibrations.[38−40] Peaks at around 1365 cm^{-1} could be ascribed to ν(C−O−C), while typical $-CH_2$ stretching vibration bands could be observed at 2845 and 2930 cm^{-1}.[27] Hydroxyl (−OH) groups formed during the process of TEOS hydrolysis appear at 3200 cm^{-1}.[38,39] The composition-induced changes in the bands around 3200 cm^{-1} indicate that the silica subnetwork becomes increasingly cross-linked with the increase of TEOS content and consumed excessive −OH groups in GPTMS. Overall, the FT-IR results suggest the formation of PTHF-SiO_2 conetworks.

The final I/O ratio in the hybrids was determined by thermogravimetric analysis (TGA) (Figure. 2b). The total inorganic weight fraction varies from 5.1% to 20.9% in the studied samples (Table 1). As observed during the TGA heating process, the organic polymers begin to degrade at ∼210 °C and are fully decomposed at 390 °C in all hybrids. X-ray diffraction (XRD) measurements are also conducted, showing that all of the hybrids are completely amorphous, as seen from the absence of any characteristic sharp diffraction peaks (Figure S3). Such noncrystallinity is in agreement with expectations, since hydrolysis, extended condensation, and covalent linkage processes effectively lead to uniform dispersion of SiO_2, which strongly hinders the effective ordering among either inorganic "SiO_4" tetrahedral or organic macromolecules into crystalline structures.[41] Furthermore, atomic force microscopy (AFM) images of the PTHF·16TEOS hybrid demonstrate a relatively uniform morphology and phase distribution on the nanoscale (see height and phase AFM images in Figure 2c).

Table 1. Compositions of PTHF·xTEOS Hybrids with Different I/O Ratios, including the Amounts of THF Monomer, Coupling Agent GPTMS, Inorganic Precursor (Hydrolyzed TEOS), and Final I/O Weight Ratio

Sample	THF monomer (mL)	GPTMS (mL)	TEOS precursor aqueous (mL)	Final I/O wt%[a]
PTHF·0TEOS	20	1.24	0	5.1/94.9
PTHF·2TEOS	20	1.24	0.60	6.8/93.2
PTHF·4TEOS	20	1.24	1.20	10.0/90.0
PTHF·8TEOS	20	1.24	2.40	12.8/87.2
PTHF·16TEOS	20	1.24	4.80	20.9/79.1

[a] Determined from TGA data (see Figure 2b).

Considering the structure of the silica subnetwork, we have investigated the differences induced by I/O ratio variations through solid state ^{1}H, ^{13}C, and ^{29}Si nuclear magnetic resonance (NMR) spectroscopy measurements (Figure 2d−f, S6). First, regarding the coupling agent (GPTMS) used in the experiment, the T^3 structure represents fully condensed −C−Si−(O−Si−)$_3$ moieties.[42] In comparison, T^1 and T^2 structures refer to partially condensed units with two and one −O−Si bonds connected to Si, respectively.[43] For the silica structure hydrolyzed from TEOS, the fully cross-linked structure is defined as Q^4 with four siloxane bonds.[16,42] The molecular structures of T^3 and Q^4 are illustrated in Figure S4. As depicted in Figure 2d, with the increase in the content of TEOS, the fraction of Q-type structures increases while the fraction of T^2 decreases, indicating the presence of more branched structures.

Regarding the organic polymer subnetwork, we consider ^{13}C NMR spectra, which are dominated by the PTHF-related peaks at 26.5 and 70.4 ppm (Figure 2e). This is consistent with literature data for poly(tetramethylene oxide), which is a structural analogue of PTHF.[44−46] Almost undetectable peaks (at 58 and 15 ppm in Figure 2e) indicate a very low fraction of alkoxide functionality as ending groups, suggesting a small fraction of unhydrolyzed GPTMS and/or TEOS. Moreover, through analysis of the ^{1}H NMR data, we find that with the increase in the content of TEOS a slight increase in the shielding of both the methylene protons (H_a and H_b in Figure S5) in the PTHF segment is observed (see Figures 2f and S6). Such a smaller deshielding effect from the oxygen atom in oxymethylene moiety on both H_a and H_b nuclei indicates enhanced intermolecular interactions between the silanol and oxymethylene moieties in the hybrids with higher TEOS

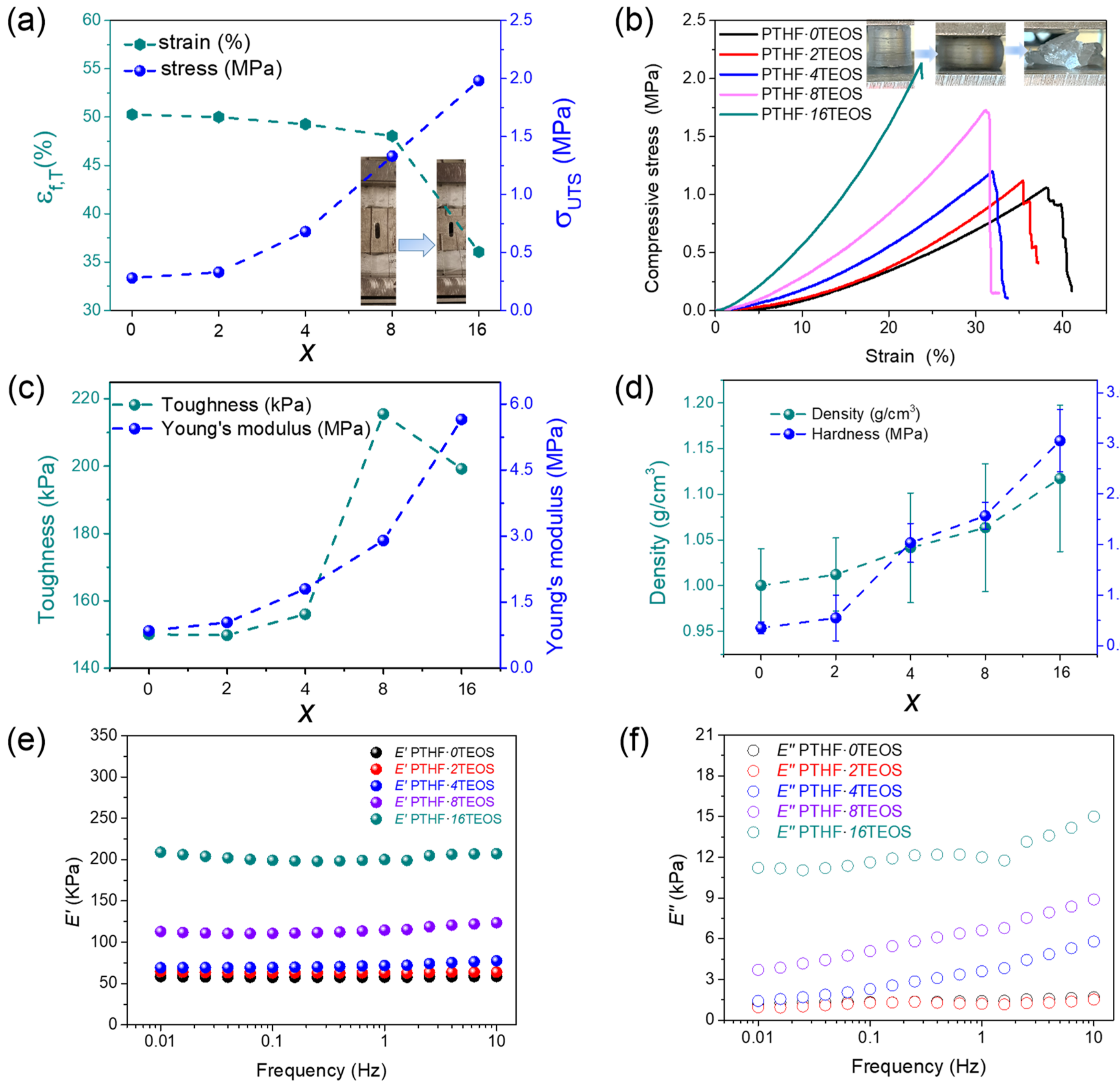

Figure 3. Mechanical properties of PTHF·*x*TEOS hybrids with different I/O weight ratios. (a) Ultimate tensile strength (σ_{UTS}) and tensile strain at failure ($\varepsilon_{f,T}$) as obtained from uniaxial tensile measurement as a function of TEOS content. (b) Stress−strain curves from compression test. (c) Modulus of toughness and Young's modulus as a function of TEOS content. (d) Density and hardness from microindentation test as a function of TEOS content. (e) Storage modulus (E') and (f) loss modulus (E'') as a function of frequency.

content. Moreover, we find a well-pronounced increase in the FWHM (full width at half-maximum) of both resonance peaks of H_a and H_b with higher TEOS content. This behavior reveals pronounced noncovalent interactions among organic/organic and organic/inorganic phases, restricting the "free-rotation" of methylene C−C bonds, and therefore leads to broader peaks related to these two methylene hydrogen atoms.

The variations in the protons' chemical shifts with hybrid composition could be attributed to (i) higher TEOS content, resulting in higher degree of cross-linking of the silica subnetwork; (ii) organic PTHF becomes more entangled within the silica subnetwork; (iii) intermolecular H-bonding between silanols and H-nuclei becomes more pronounced; and/or (iv) H-nuclei become more deshielded, having lower electron density. In other words, the peaks are shifted to lower fields based on how dense the network is, *i.e.*, how much TEOS has been added.

Based on the apparent flexibility of the samples observed during their handling (see step 4 in Figure 1b), we expect the hybrids to be able to undergo significant permanent deformation without fracturing. To quantify such mechanical properties of the hybrids, we have performed systematic studies of the influence of I/O ratio on the mechanical performances. Uniaxial tensile tests performed on rectangular specimens are compared in Figure 3a, with the extent of ultimate strain decreasing from 50.0% to 35.2% with the increase of the inorganic content in the hybrid from 5.1% to 20.9%. Simultaneously, the failure strength increases from 0.32 to 1.35 MPa. Thus, the hybrids with a higher content of inorganic silica exhibit less flexibility and elastomeric deformation behavior.

Stress−strain curves from uniaxial compression tests on cylindrical monolith bulk PTHF·*x*TEOS hybrids are shown in Figure 3b. A larger polymer content in the hybrids results in larger deformation and a lower level of ultimate stress, showing that such hybrids are more ductile compared with the inorganic-rich hybrids. The hybrid PTHF·0TEOS can be compressed to 38.3% of its original height at a stress of 1.06

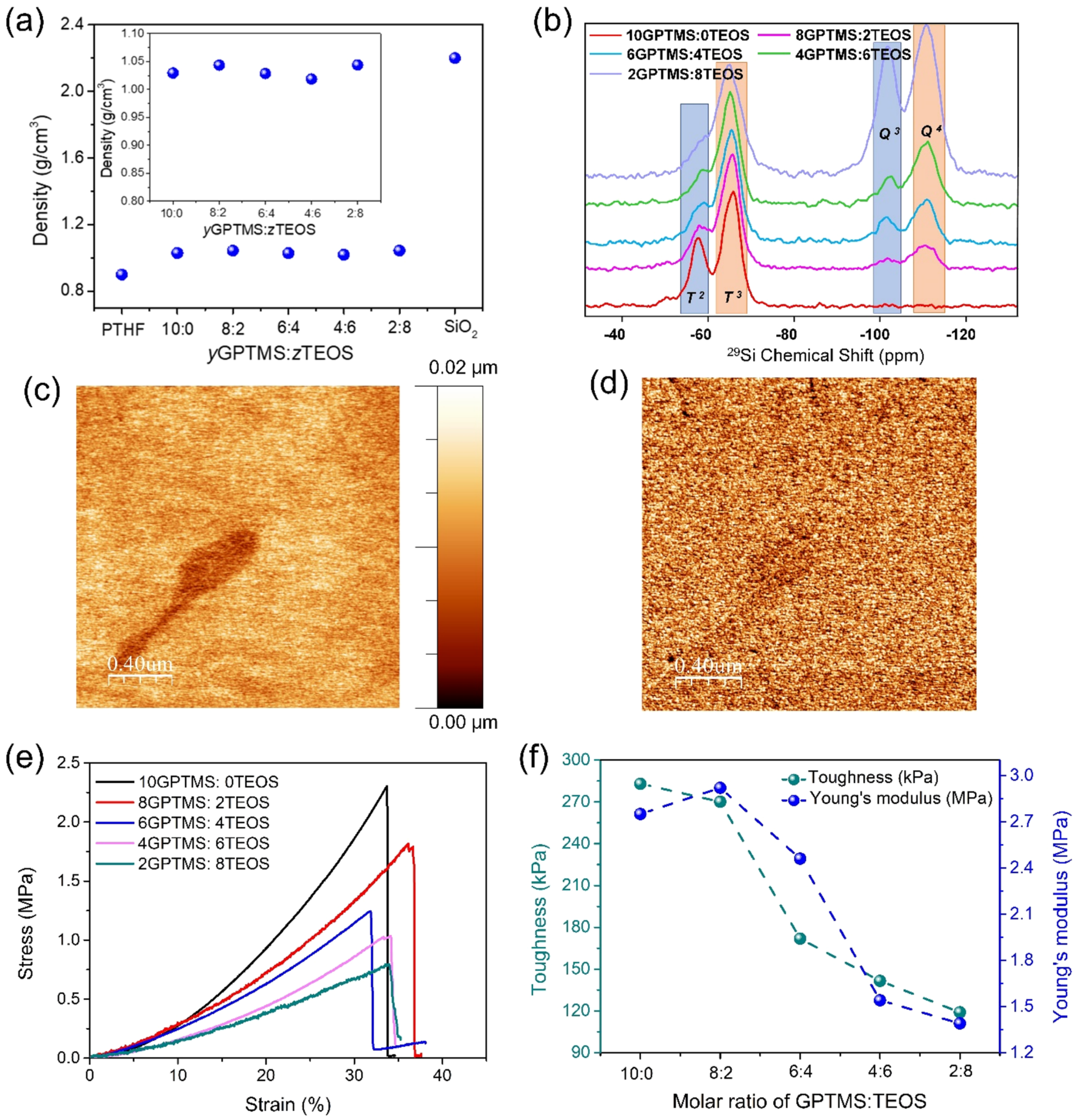

Figure 4. (a) Composition dependence of density of *y*GPTMS:*z*TEOS hybrids, pure PTHF, and pure silica glass. (b) Solid-state ^{29}Si CPMAS NMR spectra of *y*GPTMS:*z*TEOS hybrids. (c) Height and (d) phase AFM images of the 2GPTMS:8TEOS hybrid. (e) Stress−strain curves of *y*GPTMS:*z*TEOS hybrids from compression test. (f) Composition dependence of modulus of toughness and Young's modulus for *y*GPTMS:*z*TEOS hybrids.

MPa and then fractures, while PTHF·16TEOS ruptures at 23.7% of its original height at a stress of 2.14 MPa under the same loading conditions. The compression processes are illustrated in the insets of Figure 3b.

Achieving a good balance between strength and toughness is a major challenge. As seen from Figure 3a,b, with the increase of TEOS content, the failure strain of hybrids decreases while the strength increases. However, in order to function as tissue scaffolds and accommodate cyclic loading, hybrids with both desirable strength and toughness are required. We here achieve such balance in the PTHF·8TEOS hybrid, which not only reveals desirable elongation (31% for compression) and good flexibility but also high strength at 1.75 MPa. It also features the highest compressive toughness as can be seen in Figure 3c. At higher TEOS content, the elongation and toughness sharply drop. Such balancing of strength and toughness by controlling the I/O weight ratios is achieved through size of the inorganic nanoparticles, intermolecular interactions, and chain frictions.

We have further evaluated the modulus of toughness (*U*) and Young's modulus (*E*) through the area under the compression stress−strain curves and the slopes of the initial linear elastic portion of the stress−strain curve in Figure 3b, respectively.[47] The results are summarized in Figure 3c, showing that *U* and *E* are positively correlated to the SiO_2 content in the hybrids. For the hybrid PTHF·0TEOS, *U* and *E* are 150.0 kPa and 0.85 MPa, respectively, while they are 199.2 kPa and 5.65 MPa, respectively, for hybrid PTHF·16TEOS. Considering the five hybrids in the PTHF·*x*TEOS series, PTHF·8TEOS reveals the highest *U* of 219 kPa, again highlighting the good mechanical properties of this material.

Such balance of strength and toughness through controlling the I/O weight ratio of hybrid materials could guide further materials designing. As to the improvement in mechanical

https://doi.org/10.1021/acsnano.2c03440

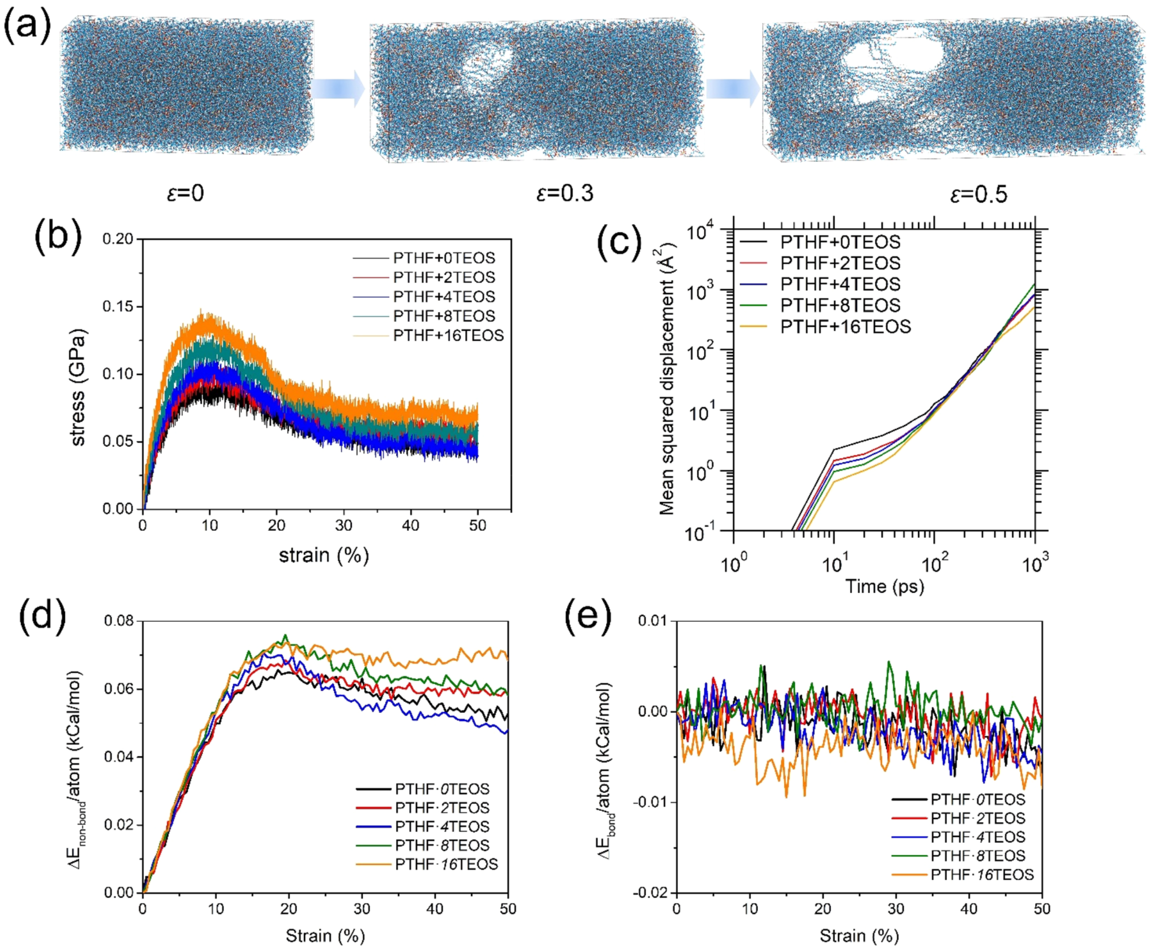

Figure 5. (a) Simulated fracture evolutions of PTHF·8TEOS hybrids by means of CVFF potential under the elongation at the strains of $\varepsilon = 0$, 0.3, and 0.5. The simulation box has dimensions of around 200 × 100 × 100 Å. (b) Simulated stress–strain curves of PTHF·*x*TEOS-based hybrids. (c) Time-dependence of the mean squared displacement of Si atoms in PTHF·*x*TEOS-based hybrids during the tensile process. Variation in the simulated potential energy of PTHF·*x*TEOS hybrids as a function of the applied strain, as decomposed into (d) nonbonded and (f) bonded energy.

properties, it can be explained by the formation of more cross-linked $-SiO_2-$ units as the I/O ratio increases. The hybrids show less elongation at fracture but at a higher stress, transforming from a rubber-like (polymer dominated) to a glass-like state (silica dominated). These changes in mechanical performance are supported by the ^{29}Si CPMAS NMR results (Figure 2d), showing that the silica subnetwork becomes more cross-linked and condensed with the increase of TEOS content, resulting in higher stress needed for deformation. The density (ρ) of the hybrids also increases with the addition of more silica, namely from 1.00 g/cm^3 for hybrid PTHF·0TEOS to 1.12 g/cm^3 for hybrid PTHF·16TEOS, *i.e.*, an increase of 12% (Figure 3d). Vickers microhardness (H_V) also increases with higher silica content from 0.8 MPa for PTHF·0TEOS to 3.0 MPa for PTHF·16TEOS (Figure 3d).

In order to investigate the dependence of I/O weight ratio on the hybrids' viscoelastic properties, dynamic mechanical analysis (DMA) measurements were performed.[48] The results of sweep frequency show that the storage modulus (E') (Figure 3e) of the five hybrids is 15 to 30 times higher than the corresponding loss modulus (E'') (Figure 3f), confirming the formation of elastic solid hybrids.[25,49] We also note that no significant changes in E' and E'' values could be observed in any of the hybrids over the tested frequency range (0.01−10 Hz), indicating a rubber plateau like behavior and cross-linked structures of the hybrid networks.[50] The values of tan (δ) equal to E''/E' are ≤0.06 for all five hybrids at 1 Hz (Figure S7), representing elastic properties of the hybrid materials.

Experimentally Produced Hybrids with Different Silica Size. To investigate the role of the silica domain size on the mechanical properties, we have prepared PTHF-based hybrids with different molar ratios of GPTMS to TEOS. GPTMS as the coupling agent is the only bridge to link PTHF polymer chains and hydrolyze TEOS, and therefore, the [GPTMS]/[TEOS] ratio controls the size of silica particles in the system. Namely, for a constant total I/O ratio, fewer but larger silica nanoparticles are obtained as [GPTMS]/[TEOS] decreases and *vice versa*.

TGA measurements are performed to determine the final I/O weight ratio of *y*GPTMS:*z*TEOS (10:0, 8:2, 6:4, 4:6, 2:8) hybrids, as shown in Figure S8. The results confirm very similar I/O values for the five hybrids. The density data of the *y*GPTMS:*z*TEOS hybrids are shown in Figure 4a, which also show limited variation. Thus, the size of silica particles has only a minor impact on density compared to the variation in the total I/O ratios (Figure 3d). The molecular structures of the *y*GPTMS:*z*TEOS hybrids are probed by FT-IR spectroscopy

(Figure S9). Typical signals of these five *y*GPTMS:*z*TEOS hybrids for Si−O (at 490 and 1090 cm^{-1}) and C−O (at 1365 cm^{-1}) are observed due to their similar chemical compositions. ^{29}Si CPMAS NMR spectroscopy is also performed on these samples to confirm the silica structures (Figure 4b). For the 10GPTMS·0TEOS hybrid, *Q*-type silane signals are not observed at any significant fraction, while T^3-type structure is dominant, since no TEOS exists in this hybrid. With the increase in content of TEOS, the intensity of the *Q*-type signals increases, indicating that the silica network becomes more cross-linked. AFM height and phase images of hybrid 2GPTMS:8TEOS are shown in parts c and d, respectively, of Figure 4, revealing the uniformity of the two phases and surface morphology of the sample at the nanoscale. All hybrids in this series are also fully X-ray amorphous as expected (Figure S10), since they also undergo sol−gel condensation process.

To confirm that we can control the size of silica particles, SEM and EDX studies have been conducted as shown in Figure S11. As observed, the representative size of single silica NPs (not their aggregates) in hybrid 2GPTMS:8TEOS and 4GPTMS:6TEOS reaches 300−400 nm, while those in hybrid 6GPTMS:4TEOS and 8GPTMS:2TEOS are around 100 nm. For the hybrid 10GPTMS:0TEOS, the silica NPs are much smaller and uniformly dispersed in the material.

As to the mechanical properties, we first consider the results of the compression tests. As shown in Figure 4e, the stress at failure of the hybrids decreases with the decrease of GPTMS, for example, 2.34 MPa for 10GPTMS:0TEOS and 0.75 MPa for 2GPTMS:8TEOS. On the other hand, the conventional strain to failure features only minor differences (within the range of 32−37%). Toughness and Young's modulus, as calculated from these stress−strain curves, follow the same trend as stress with the change in composition (Figure 4f). Thus, stress at failure, toughness, and Young's modulus highly depend on the size of the silica nanoparticles in the hybrid, while the deformation ability (ultimate strain) appears to be largely related to the polymer content. Smaller silica nanoparticles give rise to more uniform dispersion in the system, which increases the possibility of sufficient intermolecular interactions between Si−O bond in the inorganic network and C−O−C bond of polymer chains. In this way, stronger hybrids can be obtained for much smaller silica nanoparticles in the system, while hybrids with more ductile deformation can be obtained for higher polymer content. Such strategy involving control on both inorganic *vs* organic weight ratios and NP sizes reveal improved properties with breakage strain of 34% and stress of 2.32 MPa. This is an improvement compared to previous work on similar compositions, exhibiting breakage strain and stress of 26% and 1.24 MPa, respectively.[27]

MD Simulation and Predicting. The above experimental results were combined with MD simulations to better understand the deformation and fracture mechanisms of the hybrids. We focused on hybrids with different I/O ratio (PTHF·*x*TEOS series) from the experiments, as they exhibited a good balance of strength and toughness. The simulations are done using a classical Consistent Valence Force-Field (CVFF) potential (see the Methods in the Supporting Information). As shown in Figure 5a, the simulated PTHF·8TEOS hybrid with a good strength-toughness balance in experiments exhibits a fairly ductile response upon deformation at the nanoscale, which manifests itself by the continuous stretching and disentanglement of the polymer chain from the matrix upon tension. The basic structural units of hybrids with different I/O ratios are depicted in Figure S12, and the corresponding fracture simulations of the different hybrids are shown in Figure S13.

As the utilized CVFF potential does not allow for explicit bond-breaking processes, we have validated this approach through a similar tensile fracture simulation of the PTHF·8TEOS hybrid using a reactive (ReaxFF) potential, which accounts for bond-breakage and bond-formation processes. Overall, this reactive simulation confirms the tensile simulation of the CVFF simulation (see Figure S14). In detail, due to the higher computational cost of the ReaxFF simulation, we have reduced the simulated system size by 20% compared to that of CVFF; *i.e.*, it consists of 20 structural units. Interestingly, despite the reactive nature of ReaxFF, the structural units of the hybrids persist during the tensile process, indicating that the failure of the hybrids is indeed attributed to the disentanglement of the polymer chains rather than their breakage (see Figure S14a). When comparing the stress−strain responses based on these two types of simulation potentials, we find that both predict the nanoductile features of the hybrids. Additionally, good agreement between the predicted maximum stress and corresponding strain by the two potentials is observed (Figure S14). Therefore, we adopt the CVFF potential for the following simulations as it allows for larger system size and longer time scales.

To further understand the effect of the I/O ratio on mechanical properties and also investigate the role of the polymer repeating unit, we include comparison of PTHF·*x*TEOS and PTHP·*x*TEOS hybrid series in the MD simulations. Peaks in the simulated pair distribution functions of the PTHF−SiO_2 and PTHP−SiO_2 hybrids at intramolecular−atomic distances of 0.95, 1.10, 1.45, 1.53, and 1.60 Å are attributed to the O−H, C−H, C−O, C−C, and Si−O pairs, respectively, corresponding to those of covalent bonds (Figure S15). Therefore, the short-range structures (first coordination shell) of the different hybrids are fairly similar. The simulated stress−strain curves of PTHF·*x*TEOS and PTHP·*x*TEOS hybrid series are presented in Figure 5b and Figure S17, respectively. We observe that all of the hybrids exhibit a ductile response upon tension at the nanoscale, which is attributed to the high covalent bond strengths and possibility for structural rearrangements. The maximum stress increases with an increase in the content of the SiO_2 nanoparticles for both PTHF·*x*TEOS (Figure 5b) and PTHP·*x*TEOS (Figure S17) hybrids, which echoes the experimental observations of SiO_2 strengthening shown in Figure 3b. Interestingly, the strain at the maximum stress (yield stress) is constantly around 10% for all samples. As shown in Figures 5c and S16, the averaged mean squared displacement of Si atoms decreases at the early stage of tension (*i.e.*, for strain <20%) with an increase of the TEOS amount, indicating that the hybrids are more rigid when they are constructed as higher SiO_2 content. We also notice that the evolution of potential energy terms (*i.e.*, bonded term and nonbonded term) exhibit different trends upon tension (see Figures 5d,e and S18). That is, the nonbonded term consisting of van der Waals and Coulombic terms exhibits much larger changes compared to the bonded term, which further confirms that the deformation and fracture of the hybrids is controlled by the intermolecular interaction, *i.e.*, the slippage and disentanglement of the polymer chains. The strengthening mechanism can be attributed to the fact that the

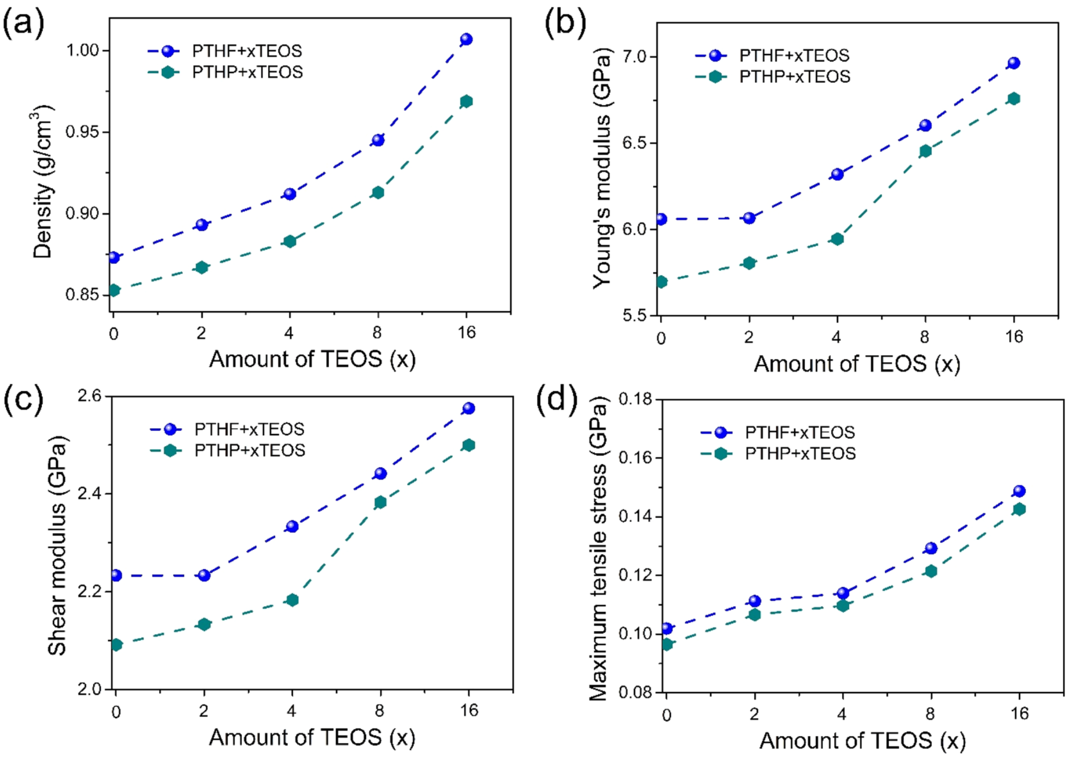

Figure 6. Composition dependence of simulated (a) density, (b) Young's modulus, (c) shear modulus, and (d) maximum tensile stress for PTHF·*x*TEOS and PTHP·*x*TEOS series of hybrids.

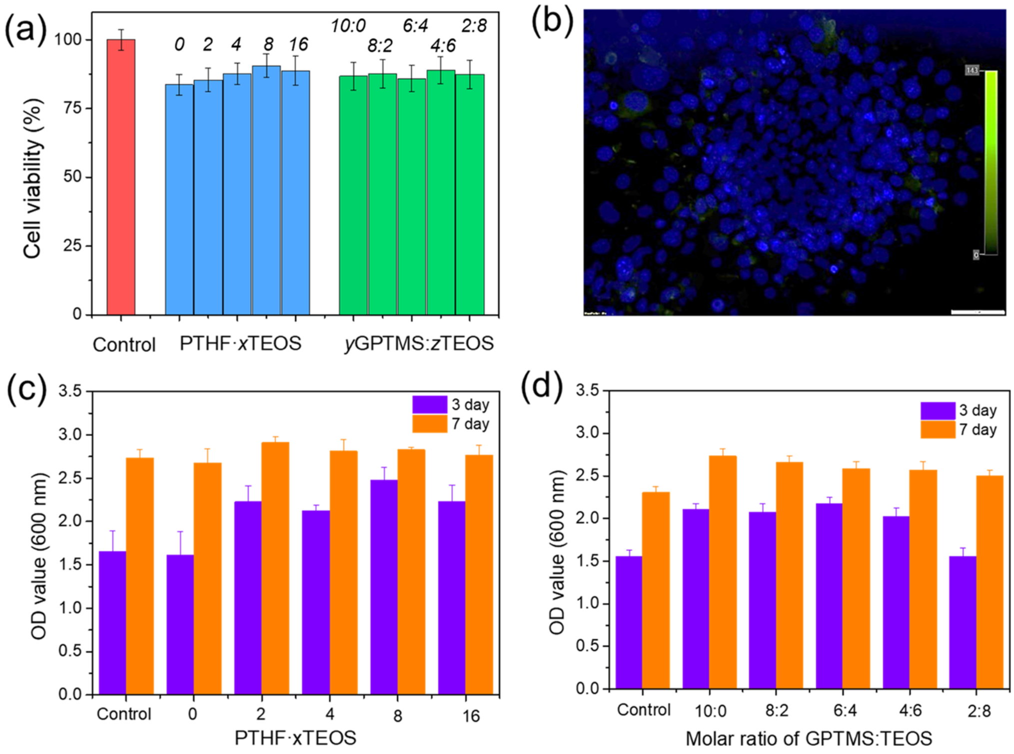

Figure 7. (a) Assessment of cell viability of hybrids by ToX8 metabolic activity assay following ISO 10993 standards. (b) Immunohistochemical staining of the nuclei of MC3T3-E1 cells cultured on PTHF·8TEOS hybrid. (c, d) Cell proliferation of MC3T3-E1 cells on (c) PTHF·*x*TEOS and (d) *y*GPTMS:*z*TEOS hybrids after culturing for 3 and 7 days.

existence of SiO_2 nanoparticles in the hybrids can effectively block the motion of polymer chains upon deformation.

The effects of TEOS content (*i.e.*, I/O ratio) for the two different repeating unit of polymer chains (PTHF *vs* PTHP) on the mechanical properties of the simulated hybrids are summarized in Figure 6. As shown in Figure 6a, density increases with an increase in the TEOS amount for both hybrid series, but the density of the PTHF·*x*TEOS hybrid series is always higher than that of the PTHP·*x*TEOS for each value of *x*. That is, density decreases with the ratio of C−O− to C−C bonds. This trend agrees well with the experimental results shown in Figure 3d. The simulated Young's modulus, shear modulus, and maximum (yield) strength also exhibit the same trend as the experimental results (see Figure 6b−d), indicating the transition from rubber-like to glass-like behavior with increasing size and fraction of SiO_2. Despite reproducing the qualitative trends, we also note that the simulated strength and modulus values are systematically higher than the experimental ones, which can be attributed to the following reasons: (i) the polymer chain lengths in the experimental samples exhibit a broad distribution, but they are simplified as a monodispersed length in the simulations; (ii) defects exist in the experimental specimens, while the simulated structures are ideally flawless; and (iii) the strain rate in the loading simulation is much higher than that in the experiments. In the meantime, it is noted that the mechanical performances of both Young's modulus and tensile strength for the PTHF−SiO_2 hybrid are better than those for the PTHP−SiO_2 hybrid. This can be attributed to the improved intermolecular interactions of PTHF−SiO_2 relative to PTHP−SiO_2 due to the higher amount of the more polar C−O functional groups (with stronger dipole moments) relative to C−C groups. Moreover, the MD simulations also reveal that van der Waals interactions are found to be the main contribution of noncovalent interactions in the hybrids compared with Coulombic interactions (Figure S19). Given the comparable stress−strain curves obtained from CVFF and ReaxFF potentials, the simulated values are also in agreement with the existing literature data for similar systems.[33,35,51] Overall, the simulations thus confirm that the content of SiO_2 nanoparticles plays an important role in controlling the mechanical properties.

Biocompatibility and Cell Growth. In addition to showing promising mechanical properties for applications within bone regeneration and tissue repairing, such hybrid materials also need to exhibit cyto-compatibility for promoting osteogenic cell attachment.[8,13] First, we have investigated the cytotoxicity of the two experimental series of hybrids. Based on the ISO 10993 standard, the materials are considered noncytotoxic if the cell viability is higher than 70% compared with the blank.[14,52] As can be seen in Figure 7a for the PTHF·*x*TEOS (*x* increases from left to right) and *y*GPTMS:*z*TEOS (*y*:*z* decreases from left to right) experimentally produced hybrids, the cell viabilities are all above 70%, ranging from 83 to 90% compared with the control group, demonstrating the noncytotoxicity of these hybrids. They are thus promising candidates for further cell attachment, proliferation, and even *in vivo* studies. To this end, we next determined the bone cell (MC3T3-E1) attachment of the hybrid materials by immunohistochemistry and confocal microscopy measurements after culturing the cells for 72 h.[22,27] As seen from the DAPI nuclear counter staining method results in Figure 7b for the PTHF·8TEOS hybrid, cells are well attached on the material, demonstrating biocompatibility of hybrids and potential for growth of bone cells. Finally, we studied the cell proliferation possibility on the hybrids *via* the ToX8 method. Bone cells cultured on PTHF·*x*TEOS and *y*GPTMS:*z*TEOS hybrids are compared with control groups in Figure 7c,d, respectively, by determining optical density (OD) values.[53] The cells seem to have better growth on hybrids relative to the control, demonstrating that these biocompatible hybrids possess excellent performance for promoting MC3T3-E1 cell growth. This could be because the silica networks can offer enhanced cell recognition sites and further improve the cell attachment and growth.[27] After culturing for 3 days, the cell number increases in samples with higher content of inorganic component, which might be because the uniform dispersion of inorganic−organic phases and adequate cross-linking networks help promote cell proliferation. Thus, based on these results, the PTHF-SiO_2 based hybrids reveal the necessary mechanical and biomedical properties for acting as desirable bone repair scaffolds.

CONCLUSIONS

Based on the experiments and MD simulations performed in this study, noncovalent intermolecular interactions are found to play an important role in controlling the deformation and fracture of inorganic−polymer hybrid materials. By decreasing the silica nanoparticle size and increasing the fraction of C−O bonds in polymer chains, the interactions between polymer chains and silica networks can be enhanced. Importantly, by further controlling the total I/O ratio the important balance of the toughness and strength can be tailored. Namely, the hybrid PTHF·8TEOS achieves a balance between these otherwise conflicting performances, showing 31% of compressive deformation, 1.75 MPa of stress at breakage, and 219 kPa of toughness. Moreover, the prepared hybrids all show non-cytotoxicity and the ability to support cell attachment as well as cell proliferation in the *in vitro* studies. These insights suggest the potential use of especially the PTHF·8TEOS hybrid material for engineering applications such as tissue scaffolds and soft robotics.

EXPERIMENTAL METHODS

Materials. Tetrahydropyfuran (THF), (3-glycidoxypropyl) trimethoxysilane (GPTMS), boron trifluoride-diethyl ether ($BF_3·OEt_2$), tetraethyl orthosilicate (TEOS), acetic acid glacial ≥99.7%, and HCl (36 wt %) were all purchased from Sigma-Aldrich and used as received. Cell culture reagents were purchased from Invitrogen and Sigma-Aldrich UK. The MC3T3-E1 preosteoblast cell line (ATCC, UK) was cultured in basal α-MEM supplemented with 10% (v/v) FCS (fetal calf serum) and 1% (v/v) penicillin. Cultures were maintained in a humidified atmosphere at 37 °C, 5% CO_2, and 21% O_2. Cells were passaged upon confluence using 500 μg/mL trypsin-EDTA (ethylene diamine tetraacetic acid).

Synthesis of Inorganic sol. SiO_2 was prepared *via* hydrolysis process. TEOS, deionized water, and 36 wt % hydrochloric acid (12 M HCl) were mixed with a molar ratio of 1:3.6:0.01. The completion of the reaction was confirmed when the mixture turned from cloudy to clear.

Synthesis of Hybrids. The organic precursors were prepared based on an established procedure using HAc as a terminator[15] and then mixed with the inorganic sols based on the precalculated THF, GPTMS, and TEOS compositions. The mixtures were transferred into polytetrafluoroethylene molds and sealed for aging for 1 week at 40 °C. Afterward, the lids were removed gradually to allow drying for the following 3 weeks at the same temperature. Finally, disc-shaped samples were recovered from the molds and used for characterization. All samples were immersed in distilled water for 5 min and followed by filtration to remove any unreacted monomers and water-soluble byproducts.

Structure Characterization. Fourier-transform infrared (FT-IR) spectroscopy was performed to determine the functional groups in the inorganic bulk samples as well as the final hybrids by using a Bruker TENSOR II spectrometer with a Bruker Platinum attenuated total reflectance attachment in the range of 4000 to 400 cm^{-1}. All spectra were compiled from 64 consecutive scans and were baseline corrected using the vendor-supplied software OPUS.

To determine the final inorganic *vs* organic (I/O) weight ratio in the hybrids, thermal gravimetric analysis (TGA) was performed on a STA 449C (Netzsch) instrument. The hybrid samples were cut into small pieces and heated under a flow of air at the rate of 10 °C min^{-1}, from room temperature to 800 °C. The recorded weight loss could be ascribed to the combustion of the organic phase. The silica nanoparticles' size and element distribution in the hybrids were tested by scanning electron microscopy (SEM) using a Zeiss Gemini SEM 500 instrument at 5 kV/10 μA.

To confirm the noncrystalline structure of the hybrid materials, X-ray diffraction (XRD) analysis was carried out on pulverized samples at 2θ angles from 5° to 80° using a Panalytical Empyrean diffractometer with Cu−Kα-1 radiation source and Ni-filter.

Atomic force microscopy (AFM) measurements were carried out to determine surface morphology and phase images of hybrids. The measurements were performed with an NTEGRA Aura AFM (NT-MDT, Russia) instrument, operating in tapping mode using HA_HR (ScanSens, Germany) cantilevers.

^{29}Si magic-angle spinning (MAS) NMR was conducted to confirm the silica structures in the hybrid materials. The data were collected with an Agilent DD2 spectrometer in conjunction with an Oxford 4.7 T widebore superconducting magnet with a ^{29}Si resonance frequency of 39.70 MHz. Samples were powdered and loaded into 5 mm zirconia rotors with sample spinning of 5.0 kHz. Spectra were acquired using a $\pi/6$ tip angle of 2.7 μs, a recycle delay of 180 s, averaging of 400−1900 scans, and with high-power ^{1}H decoupling during signal acquisition. ^{1}H → ^{29}Si cross-polarization magic-angle spinning (CPMAS) NMR measurements were made on the same instrument with a contact time of 3 ms between the spins, recycle delay of 5 s, and signal averaging of 40000−80000 scans. All ^{29}Si NMR data were processed with 25 Hz apodization, referenced to tetramethylsilane (TMS) at 0.0 ppm, using the GRAMS Spectroscopy Software Suite (Thermo Fisher Scientific) to plot and fit the spectra. ^{13}C MAS NMR measurements were made at 47 T (50.25 MHz resonance frequency) using an Agilent DD2 spectrometer and Oxford wide-bore superconducting magnet. Powdered samples were packed into 5 mm zirconia rotors, with sample spinning of 7.0 kHz. ^{1}H-decoupled ^{13}C MAS NMR data were acquired by the combination of a $\pi/6$ tip angle (2.0 μs), with a delay of 60 s between scans and signal averaging of 1000 to 2000 scans. ^{13}C NMR data were processed with 10 Hz line broadening and referenced to TMS at 0.0 ppm. Plotting and spectral analyses were done in the GRAMS software package. ^{1}H MAS NMR data were collected at 4.7T (199.82 MHz resonance frequency) using a 5 mm MAS NMR probe and a background suppression pulse sequence. A calibrated $\pi/2$ pulse width of 4 μs was immediately follow by two π pulses (8.0 μs each), and 64 acquisitions were made using a 5s recycle delay. ^{1}H MAS NMR data were referenced to TMS at 0.0 ppm and processed without any additional line broadening.

Property Characterization. Density measurements on the hybrid samples were conducted through the Archimedes principle using the following equation:

$$\rho_{\text{sample}} = \frac{\rho_{\text{ethanol}} \times m_{\text{sample}}^{\text{air}}}{m_{\text{sample}}^{\text{air}} - m_{\text{sample}}^{\text{ethanol}}} \tag{1}$$

Here,ρ_{ethanol} is the density of absolute ethanol, $m_{\text{sample}}^{\text{air}}$ is the weight of sample in air, and $m_{\text{sample}}^{\text{ethanol}}$ is the weight of the sample upon immersion in ethanol.

Compression tests were performed using a Zwick Z100 universal testing machine equipped with a 100 kN load cell at room temperature. Samples were punched into cylinders with a diameter of 10 mm and a length of 5 mm. The crosshead speed was set to 1 mm min^{-1}. Tensile tests were performed using a Linkam TST350 tensile testing stage equipped with a 200 N load cell at room temperature. For these measurements, the hybrid samples were cut into rectangular shapes with a length of 30 mm, a width of 10 mm, and a thickness of 2 mm, and the crosshead speed was set to 2 mm min^{-1}. Modulus of toughness (U) and Young's modulus (E) were evaluated through the area under the stress−strain curves and the slopes of the initial linear elastic portion of the stress−strain curve, respectively. Finally, dynamic mechanical analysis (DMA) was carried out using TA Instruments DMA 850. The experiments were performed in compression mode with an amplitude of 20 μm, with the frequency varied in the range from 0.01 to 10 Hz at room temperature.

Microindentation measurements were performed using a Nanovea CB500 hardness tester to determine the hardness (H). Vickers indentations with a maximum load of 0.02 N were generated to determine H, with a loading duration and dwell time of both 10 s. The loading and unloading rate were both 0.2 N min^{-1}. Measurements were performed under laboratory conditions (temperature: 23 °C; relative humidity: ∼36%). Then hardness was calculated from the force−displacement curves using the Oliver−Pharr model.[54,55]

Cytotoxicity Test. *In vitro* cytotoxicity of the hybrids was evaluated based on the ISO 10993 standard. Hybrids were immersed in α-MEM (0.2 g/mL) and stored in n incubator for over 72 h. The extract liquid was filter sterilized and supplemented with 10% (v/v) FBS prior to use in further tests. MC3T3-E1 cells were first cultured with basel α-MEM media and seeded on 96-well plate at 10^{4} cells per well, and then left to grow in incubator for 24 h. Afterward, the media was removed and incubated with α-MEM media (control group) and extracts of hybrids for another 24 h. The media was then removed and replaced with ToX-8 dilution in α-MEM media and incubated for another 4 h. The cell viability and optical density (OD) are measured by the ToX8 method according to the manufacturer's instructions. The OD was measured spectrophotometrically at 600 and 690 nm using a microplate reader. The relative cell viability (%) was calculated as follows:

$$\text{cell viability}(\%) = \frac{[A]\text{test}}{[A]\text{control}} \times 100$$

Cell Proliferation. The hybrids were all sterilized with EtOH for over 30 min and washed three times with PBS solution. Then the hybrids were immersed in PBS solution and put under UV light overnight. After pretreatment, the cells were cultured on 24-well plates and hybrids with basel α-MEM media at 5000 cells per well. The media was changed every second day. After 3 and 7 days of incubation, media was removed and replaced with ToX-8 dilution in α-MEM media and incubated for another 4 h. The optical density was measured spectrophotometrically at 600 and 690 nm using a microplate reader.

MD Simulations. To understand the atomistic deformation and fracture mechanisms of the hybrid samples, MD simulations were carried out. All of the simulations were performed using LAMMPS software with the GPU-accelerated package, and visualization of the atomic snapshots was done using the OVITO package. During the simulation, periodic boundary conditions were applied in all directions. The atomic interactions of hybrids were described using the classical Consistent Valence Force-Field (CVFF) potential.[56] For comparison and validation, we also applied the reactive force field (ReaxFF)[57] at a smaller system size (fewer number of total atoms) to simulate the mechanical response. These two force fields have been widely applied in simulating structure and mechanical properties of polymers and inorganic materials.[58,59] The motion of atoms was integrated using the velocity-Verlet algorithm with a time step of 0.5 fs.

First, we prepared the basic unit of the hybrids, *i.e.*, one polymer chain linked to a SiO_2 nanoparticle through GPTMS. To enable qualitative comparison with the experiments, we selected THF and THP as the monomer unit (MU) to vary the chain length. Each polymer chain consisted of 56 MUs. The SiO_2-to-polymer molar ratio was set to 0, 2, 4, 8, and 16, respectively, corresponding to a growing size of the SiO_2 nanoparticle. Note that each basic unit of the hybrids consisted of >700 atoms (Figure S12). We then randomly placed 100 basic units (20 basic units for the ReaxFF system, which is more computationally expensive) into a cubic box using the PACKMOL package.[7] These systems were compressed into a densified matrix under *NPT* ensemble at 300 K and 1 GPa for 200 ps, which yielded a density close to the experimental value. Afterward, the system was equilibrated at 500 K in the *NVT* ensemble for 100 ps, and gradually cooled to 300 K at a cooling rate of 0.2 K ps^{-1} in the *NPT* ensemble at zero pressure. The resulting configurations were subsequently relaxed at 300 K for 120 ps to ensure the convergence of density and potential energy. The structure of hybrids was characterized using pair distribution function, describing the probability of a pair of atoms at a given distance.

The elastic properties of the hybrids were determined by stepwise deforming the atomic hybrid models for a strain step of 0.0005. This was applied for both uniaxial and shear deformation. After each deformation step, the structure was subjected to an energy minimization and the corresponding pressure in the deformation direction was extracted. Then the stiffness matrix was obtained through the slope of the linear part of the stress−strain curve. Based on the stiffness matrix, Young's modulus and shear modulus were determined as described elsewhere.[60] The deformation and fracture behavior of the hybrid systems were investigated through uniaxial tensile simulation. To this end, we first duplicated the orthorhombic configuration in the *x*-direction so that the deformation was applied to the longest direction. Before deformation, the resulting structures were dynamically equilibrated in the *NPT* ensemble at 300 K and zero pressure for 100 ps to remove internal stresses. Then a constant strain rate of 5×10^{10} s^{-1} was applied along the *x*-direction, while the system was maintained at 300 K in the *NVT* ensemble. During the deformation, all of the atoms were forced to move in an affine transformation way; *i.e.*, the coordinates of the atoms were scaled along with box deformation. The stress component in the *x*-direction and corresponding strain were recorded to construct the stress−strain curve until the system reached a maximum strain of 50%. During the tensile process, the motion of Si atoms in the hybrids was studied by calculating the mean squared displacement (MSD) of each Si atom

$$\mathrm{MSD}_i(t) = \Delta r_i^2(t) = \langle |r_i(t+\tau) - r_i(\tau)|^2 \rangle \tag{2}$$

where $r_i(t)$ is the position of the *i*th atom at time *t* and the brackets represent the averaging over multiple time origins (τ).

ASSOCIATED CONTENT

Supporting Information

The Supporting Information is available free of charge at https://pubs.acs.org/doi/10.1021/acsnano.2c03440.

Details of characterization, illustration of chemical structures, additional experimental results, additional characterization of silica NPs, compositions of the basic units of hybrids in MD simulation (PDF)

AUTHOR INFORMATION

Corresponding Authors

Donghong Yu − *Department of Chemistry and Bioscience, Aalborg University, 9220 Aalborg, Denmark;* orcid.org/0000-0002-3035-5035; Email: yu@bio.aau.dk

Morten M. Smedskjaer − *Department of Chemistry and Bioscience, Aalborg University, 9220 Aalborg, Denmark;* orcid.org/0000-0003-0476-2021; Email: mos@bio.aau.dk

Authors

Wei Fan − *Department of Chemistry and Bioscience, Aalborg University, 9220 Aalborg, Denmark*

Tao Du − *Department of Chemistry and Bioscience, Aalborg University, 9220 Aalborg, Denmark*

Aida Droce − *Department of Chemistry and Bioscience, Aalborg University, 9220 Aalborg, Denmark*

Lars R. Jensen − *Department of Materials and Production, Aalborg University, 9220 Aalborg, Denmark*

Randall E. Youngman − *Science and Technology Division, Corning Incorporated, Corning, New York 14831, United States;* orcid.org/0000-0002-6647-9865

Xiangting Ren − *Department of Chemistry and Bioscience, Aalborg University, 9220 Aalborg, Denmark*

Leonid Gurevich − *Department of Materials and Production, Aalborg University, 9220 Aalborg, Denmark*

Mathieu Bauchy − *Department of Civil and Environmental Engineering, University of California, Los Angeles, California 90095, United States;* orcid.org/0000-0003-4600-0631

Peter Kristensen − *Department of Chemistry and Bioscience, Aalborg University, 9220 Aalborg, Denmark*

Bengang Xing − *Division of Chemistry and Biological Chemistry, School of Physical and Mathematical Sciences, Nanyang Technological University, Singapore 637371, Singapore;* orcid.org/0000-0002-8391-1234

Complete contact information is available at: https://pubs.acs.org/10.1021/acsnano.2c03440

Notes

The authors declare no competing financial interest.

ACKNOWLEDGMENTS

This work was supported by grants from the China Scholarship Council (CSC No. 201904910782) awarded to W.F. and the Marie Skłodowska-Curie Individual Fellowship under the European Union's Horizon 2020 Programme (No. 101018156) awarded to T.D. and M.M.S. We also thank Aalborg University for providing the computational resources through CLAAUDIA. M.B. acknowledges funding provided by the National Science Foundation under grants DMREF-1922167 and CMMI-1826420.

REFERENCES

(1) Ritchie, R. O. The conflicts between strength and toughness. *Nat. Mater.* **2011**, *10*, 817−822.

(2) Schamel, M.; Barralet, J. E.; Gelinsky, M.; Groll, J.; Gbureck, U. Intrinsic 3D Prestressing: A New Route for Increasing Strength and Improving Toughness of Hybrid Inorganic Biocements. *Adv. Mater.* **2017**, *29*, 1701035.

(3) Launey, M. E.; Ritchie, R. O. On the Fracture Toughness of Advanced Materials. *Adv. Mater.* **2009**, *21*, 2103.

(4) Shi, F. K.; Wang, X. P.; Guo, R. H.; Zhong, M.; Xie, X. M. Highly stretchable and super tough nanocomposite physical hydrogels facilitated by the coupling of intermolecular hydrogen bonds and analogous chemical crosslinking of nanoparticles. *J. Mater. Chem. B* **2015**, *3*, 1187−1192.

(5) Sun, J. Y.; Zhao, X.; Illeperuma, W. R.; Chaudhuri, O.; Oh, K. H.; Mooney, D. J.; Vlassak, J. J.; Suo, Z. Highly stretchable and tough hydrogels. *Nature* **2012**, *489*, 133−136.

(6) Li, X.; Wang, H.; Li, D.; Long, S.; Zhang, G.; Wu, Z. Dual Ionically Cross-linked Double-Network Hydrogels with High Strength, Toughness, Swelling Resistance, and Improved 3D Printing Processability. *ACS Appl. Mater. interfaces* **2018**, *10*, 31198−31207.

(7) Fan, W.; Jensen, L. R.; Ceccato, M.; Quaade, T. S.; Gurevich, L.; Yu, D.; Smedskjaer, M. M. Flexible inorganic-organic hybrids with dual inorganic components. *Mater. Today Chem.* **2021**, *22*, 100584.

(8) Zhao, W.; Jin, X.; Cong, Y.; Liu, Y.; Fu, J. Degradable natural polymer hydrogels for articular cartilage tissue engineering. *J. Chem. Technol. Biotechnol.* **2013**, *88*, 327−339.

(9) Setton, L. A.; Elliott, D. M.; Mow, V. C. Altered mechanics of cartilage with osSteoarthritis: human osteoarthritis and an experimental model of joint degeneration. *Osteoarthritis and cartilage* **1999**, *7*, 2−14.

(10) Hooper, J. B.; Schweizer, K. S. Theory of Phase Separation in Polymer Nanocomposites. *Macromolecules* **2006**, *39*, 5133−5142.

(11) Ogoshi, T.; Chujo, Y. Organic-inorganic polymer hybrids prepared by the sol-gel method. *Compos. Interfaces* **2005**, *11*, 539−566.

(12) Imai, Y.; Naka, K.; Chujo, Y. Reversible Formation of Interpenetrating Polymer Network Structure in Organic-Inorganic Polymer Hybrids. *Polym. J.* **1998**, *30*, 990−995.

(13) Arumugam, S.; Ju, Y. Carbon nanotubes reinforced with natural/synthetic polymers to mimic the extracellular matrices of bone - a review. *Mater. Today Chem.* **2021**, *20*, 100420.

(14) Chung, J. J.; Li, S.; Stevens, M. M.; Georgiou, T. K.; Jones, J. R. Tailoring Mechanical Properties of Sol-Gel Hybrids for Bone Regeneration through Polymer Structure. *Chem. Mater.* **2016**, *28*, 6127−6135.

(15) Zhao, X. Designing toughness and strength for soft materials. *Proc. Natl. Acad. Sci. U. S. A* **2017**, *114*, 8138−8140.

(16) Munch, E.; Launey, M. E.; Alsem, D. H.; Saiz, E.; Tomsia, A. P.; Ritchie, R. O. Tough, bio-inspired hybrid materials. *Science* **2008**, *322*, 1516−1520.

(17) Ravarian, R.; Zhong, X.; Barbeck, M.; Ghanaati, S.; Kirkpatrick, C. J.; Murphy, C. M.; Schindeler, A.; Chrzanowski, W.; Dehghani, F. Nanoscale Chemical Interaction Enhances the Physical Properties of Bioglass Composites. *ACS Nano* **2013**, *7*, 8469−8483.

(18) Fan, W.; Zhang, X.; Li, C. Functional fibrous compositions: Applications and perspectives. *Compos. Commun.* **2019**, *15*, 68−75.

(19) Norris, E.; Ramos-Rivera, C.; Poologasundarampillai, G.; Clark, J. P.; Ju, Q.; Obata, A.; Hanna, J. V.; Kasuga, T.; Mitchell, C. A.; Jell, G.; Jones, J. R. Electrospinning 3D bioactive glasses for wound healing. *Biomed. Mater.* **2020**, *15*, 015014.

(20) Zakir, M.; Ashraf, U.; Tian, T.; Han, A.; Qiao, W.; Jin, X.; Zhang, M.; Tsoi, J. K.-H.; Matinlinna, J. P. The Role of Silane Coupling Agents and Universal Primers in Durable Adhesion to Dental Restorative Materials - a Review. *Current Oral Health Reports* **2016**, *3*, 244−253.

(21) Macon, A. L. B.; Li, S.; Chung, J. J.; Nommeots-Nomm, A.; Solanki, A. K.; Stevens, M. M.; Jones, J. R. Ductile silica/methacrylate hybrids for bone regeneration. *J. Mater. Chem. B* **2016**, *4*, 6032−6042.

(22) Mahony, O.; Tsigkou, O.; Ionescu, C.; Minelli, C.; Ling, L.; Hanly, R.; Smith, M. E.; Stevens, M. M.; Jones, J. R. Silica-Gelatin Hybrids with Tailorable Degradation and Mechanical Properties for Tissue Regeneration. *Adv. Funct. Mater.* **2010**, *20*, 3835−3845.

(23) Lee, D. W.; Yoo, B. R. Advanced silica/polymer composites: Materials and applications. *J. Ind. Eng. Chem.* **2016**, *38*, 1−12.

(24) Shi, F. K.; Wang, X. P.; Guo, R. H.; Zhong, M.; Xie, X. M. Highly stretchable and super tough nanocomposite physical hydrogels facilitated by the coupling of intermolecular hydrogen bonds and analogous chemical crosslinking of nanoparticles. *J. Mater. Chem. B* **2015**, *3*, 1187−1192.

(25) Zhong, M.; Liu, X. Y.; Shi, F. K.; Zhang, L. Q.; Wang, X. P.; Cheetham, A. G.; Cui, H.; Xie, X. M. Self-healable, tough and highly stretchable ionic nanocomposite physical hydrogels. *Soft Matter* **2015**, *11*, 4235−4241.

(26) Gabrielli, L.; Connell, L.; Russo, L.; Jiménez-Barbero, J.; Nicotra, F.; Cipolla, L.; Jones, J. R. Exploring GPTMS reactivity against simple nucleophiles: chemistry beyond hybrid materials fabrication. *RSC Adv.* **2014**, *4*, 1841−1848.

(27) Tallia, F.; Russo, L.; Li, S.; Orrin, A. L. H.; Shi, X.; Chen, S.; Steele, J. A. M.; Meille, S.; Chevalier, J.; Lee, P. D.; Stevens, M. M.; Cipolla, L.; Jones, J. R. Bouncing and 3D printable hybrids with self-healing properties. *Mater. Horiz.* **2018**, *5*, 849−860.

(28) Fan, W.; Youngman, R. E.; Ren, X.; Yu, D.; Smedskjaer, M. M. Structural control of self-healing silica-poly(tetrahydropyran)-poly-(epsilon-caprolactone) hybrids. *J. Mater. Chem. B* **2021**, *9*, 4400−4410.

(29) Vidil, T.; Tournilhac, F.; Leibler, L. Control of cationic epoxy polymerization by supramolecular initiation. *Polym. Chem.* **2013**, *4*, 1323.

(30) Guo, R.; Jacob, K. I. Effect of chain length distribution on thermal characteristics of model polytetrahydrofuran (PTHF) networks. *Polymer* **2014**, *55*, 4468−4477.

(31) Nébouy, M.; de Almeida, A.; Brottet, S.; Baeza, G. P. Process-Oriented Structure Tuning of PBT/PTHF Thermoplastic Elastomers. *Macromolecules* **2018**, *51*, 6291−6302.

(32) Owens, G. J.; Singh, R. K.; Foroutan, F.; Alqaysi, M.; Han, C.-M.; Mahapatra, C.; Kim, H.-W.; Knowles, J. C. Sol-gel based materials for biomedical applications. *Prog. Mater. Sci.* **2016**, *77*, 1−79.

(33) Liu, C.; Ning, W.; Tam, L. H.; Yu, Z. Understanding fracture behavior of epoxy-based polymer using molecular dynamics simulation. *J. Mol. GraphicsModell.* **2020**, *101*, 107757.

(34) To, T.; Sorensen, S. S.; Christensen, J. F. S.; Christensen, R.; Jensen, L. R.; Bockowski, M.; Bauchy, M.; Smedskjaer, M. M. Bond Switching in Densified Oxide Glass Enables Record-High Fracture Toughness. *ACS Appl. Mater. interfaces* **2021**, *13*, 17753−17765.

(35) Krishna, S.; Patel, C. M. Computational and experimental study of mechanical properties of Nylon 6 nanocomposites reinforced with nanomilled cellulose. *Mech. Mater.* **2020**, *143*, 103318.

(36) Hench, L. L.; West, J. K. The sol-gel process. *Chem. Revi.* **1990**, *90*, 33−72.

(37) Kotz, F.; Schneider, N.; Striegel, A.; Wolfschlager, A.; Keller, N.; Worgull, M.; Bauer, W.; Schild, D.; Milich, M.; Greiner, C.; Helmer, D.; Rapp, B. E. Glassomer-Processing Fused Silica Glass Like a Polymer. *Adv. Mater.* **2018**, *30*, No. e1707100.

(38) Rubio, F.; Rubio, J.; Oteo, J. L. A FT-IR Study of the Hydrolysis of Tetraethylorthosilicate (TEOS). *Spectrosc. Lett.* **1998**, *31*, 199−219.

(39) Matos, M. C.; Ilharco, L. M.; Almeida, R. M. The evolution of TEOS to silica gel and glass by vibrational spectroscopy. *J. Non-Cryst. Solids* **1992**, *147−148*, 232−237.

(40) Li, H.; Tripp, C. P. Infrared study of the interaction of charged silica particles with TiO2 particles containing adsorbed cationic and anionic polyelectrolytes. *Langmuir* **2005**, *21*, 2585−2590.

(41) Du, J.; She, X.; Zhu, W.; Yang, Q.; Zhang, H.; Tsou, C. Super-tough, anti-fatigue, self-healable, anti-fogging, and UV shielding hybrid hydrogel prepared via simultaneous dual in situ sol-gel technique and radical polymerization. *J. Mater. Chem. B* **2019**, *7*, 7162−7175.

(42) Glaser, R. H.; Wilkes, G. L.; Bronnimann, C. E. Solid-state 29Si NMR of TEOS-based multifunctional sol-gel materials. *J. Non-Cryst. Solids* **1989**, *113*, 73−87.

(43) Artaki, I.; Bradley, M.; Zerda, T. W.; Jonas, J. NMR and Raman study of the hydrolysis reaction in sol-gel processes. *J. Phys. Chem.* **1985**, *89*, 4399−4404.

(44) Schmidt, A.; Veeman, W. S.; Litvinov, V. M.; Gabriëlse, W. NMR Investigations of In-Situ Stretched Block Copolymers of Poly(butylene terephthalate) and Poly(tetramethylene oxide). *Macromolecules* **1998**, *31*, 1652−1660.

(45) Litvinov, V. M.; Bertmer, M.; Gasper, L.; Demco, D. E.; Blümich, B. Phase Composition of Block Copoly(ether ester) Thermoplastic Elastomers Studied by Solid-State NMR Techniques. *Macromolecules* **2003**, *36*, 7598−7606.

(46) Xu, Q.; Chen, J.; Huang, W.; Qu, T.; Li, X.; Li, Y.; Yang, X.; Tu, Y. One Pot, One Feeding Step, Two-Stage Polymerization Synthesis and Characterization of (PTT-b-PTMO-b-PTT)n Multiblock Copolymers. *Macromolecules* **2013**, *46*, 7274−7281.

(47) Liu, C.; Morimoto, N.; Jiang, L.; Kawahara, S.; Noritomi, T.; Yokoyama, H.; Mayumi, K.; Ito, K. Tough hydrogels with rapid self-reinforcement. *Science* **2021**, *372*, 1078−1081.

(48) Costa, C. S. M. F.; Fonseca, A. C.; Serra, A. C.; Coelho, J. F. J. Dynamic Mechanical Thermal Analysis of Polymer Composites Reinforced with Natural Fibers. *Polym. Rev.* **2016**, *56*, 362−383.

(49) Pillai, K. V.; Renneckar, S. Dynamic mechanical analysis of layer-by-layer cellulose nanocomposites. *Ind. Crops Prod.* **2016**, *93*, 267−275.

(50) Zandraa, O.; Jelínková, L.; Roy, N.; Sáha, T. s.; Kitano, T.; Saha, N.; Zatloukal, M. Viscoelastic Properties and Morphology of Mumio-based Medicated Hydrogels. *AIP Conf. Proc.* **2011**, *261*, 1375.

(51) Yu, C.; Yang, L.; Chen, H.; Qin, Y.; Wang, T.; Sun, W.; Wang, C. Microscale investigations of mechanical responses of TKX-50 based polymer bonded explosives using MD simulations. *Comput. Mater. Sci.* **2020**, *172*, 109287.
(52) ISO 10993-5, Biological evaluation of medical devices. In *Part 5: Tests for in vitro cytotoxicity*; ISO: Geneva, 2009.
(53) Teng, L.; Chen, Y.; Jin, M.; Jia, Y.; Wang, Y.; Ren, L. Weak Hydrogen Bonds Lead to Self-Healable and Bioadhesive Hybrid Polymeric Hydrogels with Mineralization-Active Functions. *Biomacromolecules* **2018**, *19*, 1939−1949.
(54) Broitman, E. Indentation Hardness Measurements at Macro-, Micro-, and Nanoscale: A Critical Overview. *Tribol. Lett.* **2017**, *65*, 23.
(55) Oliver, W. C.; Pharr, G. M. An improved technique for determining hardness and elastic modulus using load and displacement sensing indentation experiments. *J. Mater. Res.* **1992**, *7*, 1564−1583.
(56) Dauber-Osguthorpe, P.; Roberts, V. A.; Osguthorpe, D. J.; Wolff, J.; Genest, M.; Hagler, A. T. Structure and energetics of ligand binding to proteins: Escherichia coli dihydrofolate reductase-trimethoprim, a drug-receptor system. *Proteins* **1988**, *4*, 31−47.
(57) Newsome, D. A.; Sengupta, D.; Foroutan, H.; Russo, M. F.; van Duin, A. C. T. Oxidation of Silicon Carbide by O2 and H2O: A ReaxFF Reactive Molecular Dynamics Study, Part I. *J. Phys. Chem. C* **2012**, *116*, 16111−16121.
(58) Liu, C.; Ning, W.; Tam, L. H.; Yu, Z. Understanding fracture behavior of epoxy-based polymer using molecular dynamics simulation. *J. Mol. Graphics Modell* **2020**, *101*, 107757.
(59) Krishna, S.; Patel, C. M. Computational and experimental study of mechanical properties of Nylon 6 nanocomposites reinforced with nanomilled cellulose. *Mech. Mater.* **2020**, *143*, 103318.
(60) Martinez, L.; Andrade, R.; Birgin, E. G.; Martinez, J. M. PACKMOL: a package for building initial configurations for molecular dynamics simulations. *J. Comput. Chem.* **2009**, *30*, 2157−64.